Two-dimensional spectral analysis of mesospheric airglow image data

F. J. Garcia, M. J. Taylor, and M. C. Kelley

A technique to analyze short-period (<1 hour) gravity wave structure in all-sky images of the airglow emissions is described. The technique involves spatial calibration, star removal, geographic projection, regridding, and flat fielding of the data prior to the determination of the horizontal wave parameters (wavelength, velocity, and period), by use of standard two-dimensional Fourier analysis techniques. The method was developed to exploit the information that is now available with wide-field solid state imaging systems. This technique permits interactive and quantitative investigations of large, complex data sets. Such studies are important for investigating gravity wave characteristics, their interaction with the airglow emissions, and their geographic and seasonal variability. We study one event of this type here and present possible evidence of a nonlinear wave–wave interaction in the upper atmosphere.

Key words: Gravity waves, airglow, geographic projection, spectral estimation.

1. Introduction

It is now known that there are several airglow emission layers that result from chemiluminescent reactions of atomic and molecular species in the upper mesosphere. Table 1 lists the most prominent of these emissions in the 80–100-km height range. These emissions exhibit considerable spatial and temporal fluctuations that have been attributed to the passage of atmospheric gravity waves through the airglow layers.[1–11] Gravity waves are known to be important drivers of mesoscale fluctuations throughout the atmosphere.[12] At mesospheric heights, the waves can saturate and deposit their energy and momentum into the mean flow, a process that has been found to be an important factor that contributes to the global-scale circulation of the upper atmosphere.[13] Small-scale waves of the type readily detected by airglow imaging (exhibiting horizontal wavelengths ranging from a few to several tens of kilometers and periods of <1 hour) have been shown to contribute significantly (~70%) to the momentum budget.[14,15] Many of these waves are thought to be generated by localized disturbances within the troposphere, such as thunderstorms, deep convective regions, and fronts, and by orographic forcing resulting from winds flowing over mountains. As these waves propagate through the airglow layers, they induce significant density and temperature perturbations that affect the local chemistry and that are readily detected at ground level as line-of-sight (column) variations in the emission intensity. Various instruments, including photometers, interferometers, spectrometers and imagers, have been used to investigate this phenomenon. In particular, high resolution, solid-state (CCD) imagers are now regularly used to provide detailed information of the occurrence frequency of the waves, their horizontal wavelengths, and their apparent phase velocities.[11,16–19]

In the past most airglow imaging has been performed with relatively narrow-angle optics (typically 30°–40°).[5,8,20–24] This image format has the advantage of limited optical distortion, but it provides information on only a very restricted part of the gravity wave field. Monochromatic all-sky imaging systems have been developed for auroral and thermospheric (630.0 nm) airglow studies that provide information over a much larger field of view (180°). With improvements in CCD detectors, these systems are now capable of viewing wave structure in the mesospheric airglow emissions over a very large geographic area (up to 1,000,000 km^2 at 96-km altitude).

To investigate the morphology of these wave motions, Hapgood and Taylor[25] developed a method to

F. J. Garcia and M. C. Kelley are with the Department of Electrical Engineering, Cornell University, Ithaca, New York 14850. M. J. Taylor is with the Space Dynamics Laboratory and the Physics Department, Utah State University, Logan, Utah 84322.

Received 2 December 1996; revised manuscript received 29 May 1997.

0003-6935/97/297374-12$10.00/0

Table 1. Filter Information and Mean Heights for Airglow Emissions in Upper Mesosphere

Filter	Filter Wavelength (nm)	Filter Bandwidth (nm)	Mean Layer Height (km)
OI	557.7	2.67	~96
Na	589.2	2.37	~90
NIR OH	715–930[a]	215	~87
$O_2(0,1)$	865.5	12.0	~94
Background	572.5	2.65	–

[a]With a notch at 865 nm to suppress the O_2 (0,−1) emission.

determine horizontal wave parameters from narrow-angle image data. Lanchester[26] subsequently generalized their analysis to the all-sky image format for auroral studies. In both cases, the analysis methods relied heavily on the identification of relatively high-contrast wave patterns (or features) by the observer. Although this method has proven to be extremely useful, it does not take full advantage of the range of information that is now obtainable with solid-state imaging systems, nor does it take advantage of modern signal and image-processing tools.

All-sky monochromatic imaging systems provide high spectral sensitivity and maximum field of view for ground-based measurements, but the image format is not immediately suitable for standard two-dimensional (2-D) spectral analysis techniques. We summarize methods for processing the all-sky image data to allow these techniques to be applied. The effects of geographic projection and regridding of the data are presented together with a discussion of the limits of gravity wave parameter estimation with these data. A report that makes use of some of the techniques described here for the investigation of simultaneous wave signatures in the near-infrared OH and OI (557.7 nm) emissions has been given by Taylor and Garcia.[11]

2. Image Processing

A. Characteristics of All-Sky Images

The CCD imager we used to obtain our example images consists of a large area (6.45 cm^2), high resolution, 1024 × 1024 back-illuminated array with a pixel depth of 14 bits. The high quantum efficiency (~80% at visible wavelengths), low dark current [0.5 (electrons/pixel)/s] low readout noise (15 electrons rms), and high linearity (0.05%) of this device provide an excellent capability for quantitative measurements of the airglow emissions.[18] The camera makes use of a fast ($f/4$) all-sky telecentric lens that enables high signal-to-noise ratio (20:1) images of wave structure to be obtained with integration times of typically 15 s for the near-infrared OH emission (715–930 nm passband) and 90 s for the OI (557.7 nm) line emission. Figure 1 shows an example of gravity wave data recorded in the OI (557.7 nm) emission during the Airborne Lidar and Observations of the Hawaiian Airglow in October 1993 (ALOHA-93) campaign from Haleakala, Hawaii.[18] The image has been binned on-chip down to 512 × 512 resolution to enhance the signal-to-noise ratio.

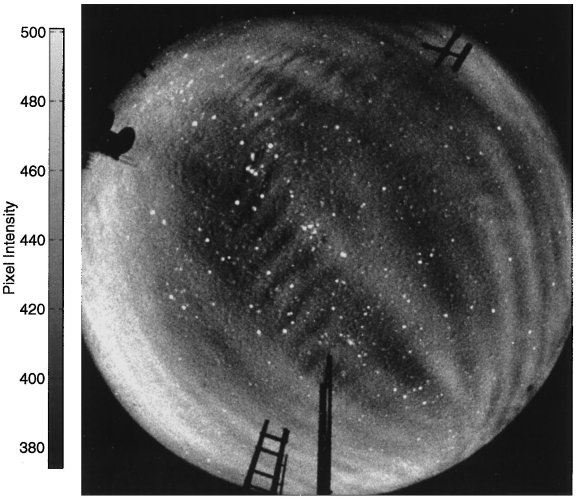

Fig. 1. 512 × 512-pixel resolution all-sky CCD image showing short-period gravity wave structure in the OI (557.7 nm) airglow emission. Data were recorded from Haleakala, Hawaii, on 22 October 1993 at 12:27 UT with a 90-s exposure.

Two linear wave patterns are evident: one large-scale wave pattern that encompasses the whole field of view while the other smaller-scale wave pattern appears in localized areas of the image (most prominently near the zenith) and is almost orthogonal to the larger-scale waves. The large-scale wave pattern illustrates the problems associated with the use of all-sky optics for airglow studies, namely that linear wave patterns appear curved and compressed at low elevation angles. This occurs because the lens projects an image onto the CCD such that each pixel subtends an equal angle of the sky. As an illustration, Fig. 2 shows the effect of projecting onto a uniform geographic grid an array of 18 × 18 super pixels that represent 10° × 10° elements of the all-sky image. The sizes of the projected pixels vary considerably with elevation, and the shapes are dependent on the viewing azimuth. Further implications of mapping the images onto a uniform geographic grid are discussed in detail in Section 2.E.

The immediate effect of this projection on the resolution is illustrated in Fig. 3(a), in which the range r along the airglow layer is shown as a function of observed elevation angle el for an OI emission layer at 96 km. The function is essentially linear for elevation angles larger than 40° (range up to 400 km), but at lower elevations the distance along the airglow layer increases rapidly, exceeding 1000 km at the horizon. Figure 3(b) shows the resulting radial (solid) and tangential (dashed) resolutions as a function of elevation angle for a 512 × 512 all-sky image. The radial resolution is the interpixel spacing that extends radially from zenith, and the tangential resolution is the interpixel spacing in the orthogonal direction. The two show similar trends at high elevations, but at low elevations the tangential resolu-

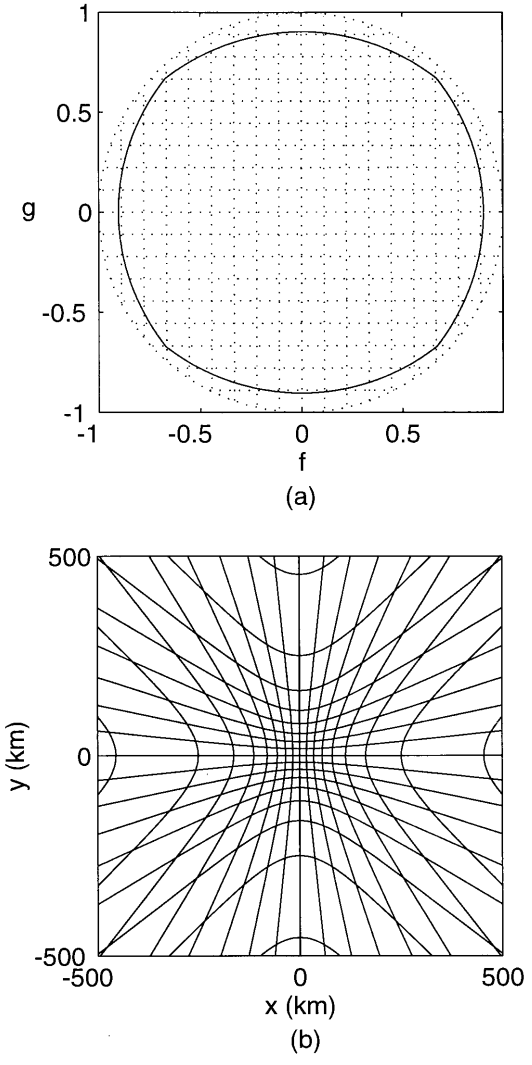

Fig. 2. Plots showing effect of projecting a pixel in the all-sky image onto a geographic coordinate system, assuming an emission height of 96 km: (a) all-sky image into 18 × 18 elements corresponding to 10° superpixels; (b) corresponding footprint of each of these superpixels is shown on a 1000 km × 1000 km area. Note the significant increase in size of the footprints at lower elevations. The solid border in (a) indicates the mapped area.

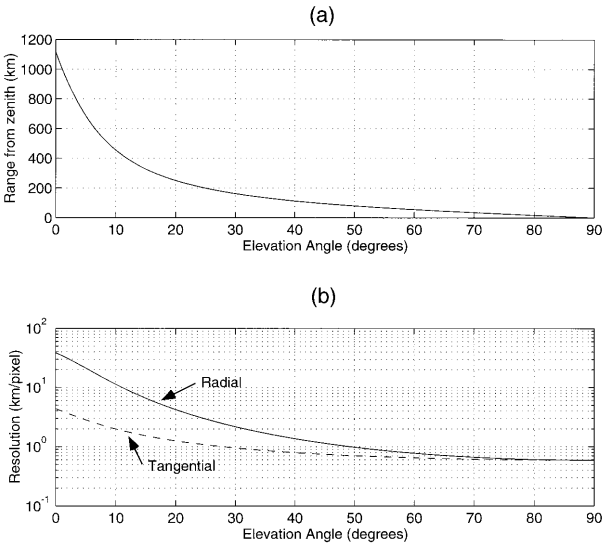

Fig. 3. Plots showing (a) variation in range from zenith along the airglow layer as a function of elevation angle for an emission height of 96 km, and (b) corresponding tangential and radial pixel resolution as a function of elevation angle for an all-sky image of 512 × 512 pixels.

tion is significantly better. The radial resolution is therefore the limiting factor for determining what portion of an image to analyze. For example, for measuring waves of horizontal wavelengths ≤20 km, the waves should be located within ~450 km of the observer (i.e., occur at >10° elevation) because at that point the radial resolution is 10 km/pixel. However, as can be seen in Fig. 11, shorter wavelengths can be observed at lower elevation angles if the waves are oriented tangentially.

Standard 2-D fast Fourier transform (FFT) analysis techniques require that the spatial resolution across the image be constant. For the example plotted in Fig. 3, the zenith resolution is 0.6 km/pixel, reducing to 1 km/pixel at ~50° elevation. Thus without additional processing, this would limit the useful area of the all-sky image to ≤30°–40° of zenith. As the data show, however, there is a considerable amount of wave information outside this range. To maximize the potential of these data, it is necessary to map the images onto a uniformly spaced grid prior to spectral analysis.

B. Coordinate Mapping

Before we can perform a quantitative analysis of the image data, it is necessary to use coordinate systems that relate distances between pixels in the image to physical distances in the airglow layer. In this section we describe the coordinate systems we used in our analysis method and show how to transform from one to another.

Figure 4 illustrates the four coordinate systems used. The original image depicts the array of data recorded by the CCD camera. The (i, j) coordinate axes represent indices in the data array. The axes are not assumed to be aligned along a specific geographic orientation. Following the method described by Hapgood and Taylor[25] for narrow-angle optics, we introduce a standard coordinate system that is a linear transformation of the original image coordinates scaled so that the horizon circle that corresponds to 0° elevation is of unit radius. The azimuth-elevation coordinate system is used to facilitate the transformation between standard coordinates and geographic coordinates. The final geographic coordinate system is a 2-D uniformly spaced grid at the height of the airglow layer. The original image is projected onto this grid to create a regularly sampled array for the 2-D FFT analysis. In this format, zenith is located at the origin of the coordinate system and the x and y axes correspond to geographic east and north, respectively. Because the airglow layer is curved (see Fig. 6), representing

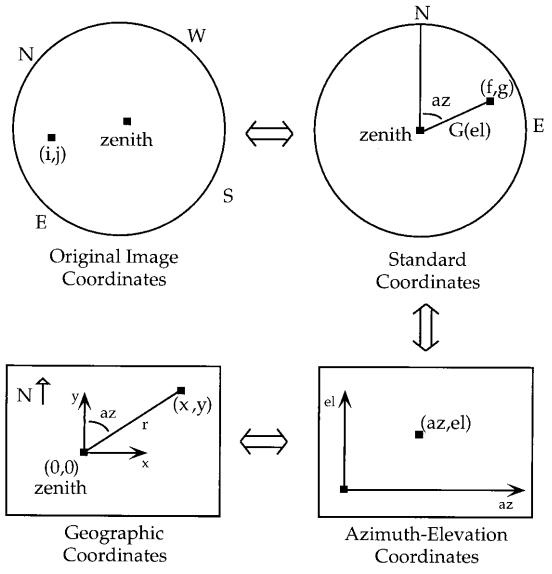

Fig. 4. Illustration showing coordinate mappings used for transforming data from the original all-sky format to geographic coordinates, and vice versa.

it on this planar grid will introduce some error; however, since the analysis area is orders of magnitude smaller than the area of the spherical shell at the height of the emission layer, this error is negligible.

Every point (i, j) in the original image corresponds to a point (f, g) in the standard coordinates, which in turn maps to a point (x, y) in geographic coordinates via the azimuth and elevation (az, el) transformation. Because each transformation is invertible, it is possible to map easily between coordinate systems:

$$(i, j) \Leftrightarrow (f, g) \Leftrightarrow (az, el) \Leftrightarrow (x, y). \tag{1}$$

The original image and the standard coordinates are related by the following linear transformation[25]:

$$\begin{bmatrix} f \\ g \end{bmatrix} = \begin{bmatrix} a_0 & a_1 & a_2 \\ b_0 & b_1 & b_2 \end{bmatrix} \begin{bmatrix} 1 \\ i \\ j \end{bmatrix}, \tag{2}$$

where the coefficients a and b are determined by spatial calibration of the image with the star background.[27]

Figure 4 illustrates the relationship between (f, g) and (az, el). This can be expressed as

$$\begin{bmatrix} f \\ g \end{bmatrix} = G(el) \begin{bmatrix} \sin(az) \\ \cos(az) \end{bmatrix}, \tag{3}$$

where $G(el)$ is determined by the format of the all-sky lens and relates elevation angle to distance, measured from the center of the image. A plot of this function for an all-sky lens (of the type used to take the image in Fig. 1) is shown in Fig. 5. We derived the function by fitting a third-order polynomial to the data supplied by the lens manufacturer. If the lens function is unknown, however, the figure shows that to a first approximation this relationship may be assumed to be linear between distance and angle.

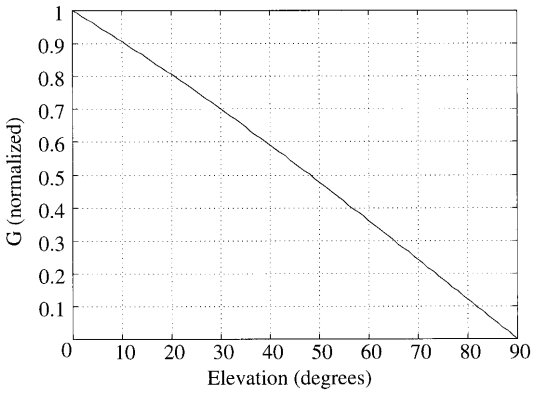

Fig. 5. Plot showing variation in the lens function G versus elevation; G is the normalized distance measured from the center of the image.

Figure 6 illustrates the airglow-observing geometry. The airglow layer is located at a mean height H above the Earth's surface. An observer at O sees structure at a point P on the airglow layer, corresponding to an elevation el above the horizon. The elevation angle is given by

$$el = \cos^{-1}\left(\frac{a \sin \alpha}{c}\right), \tag{4}$$

where

$$\alpha = (\pi - \psi)/2,$$

$$c = (H^2 + a^2 - 2Ha \cos \alpha)^{1/2},$$

$$a = 2(R + H)\sin \psi/2,$$

$$\psi = r/(R + H),$$

$$r = (x^2 + y^2)^{1/2},$$

R is the mean radius of the Earth (6370 km).

The azimuth of any point (x, y) in the geographic

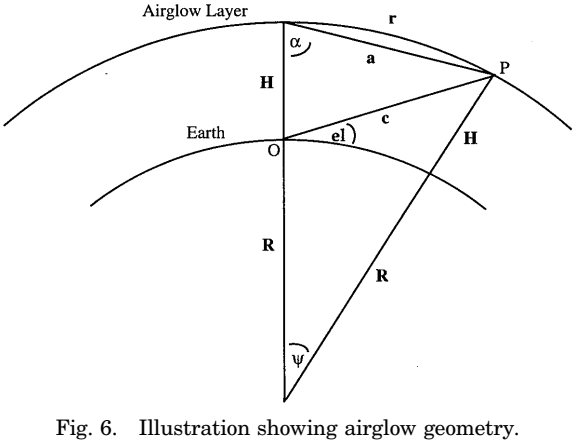

Fig. 6. Illustration showing airglow geometry.

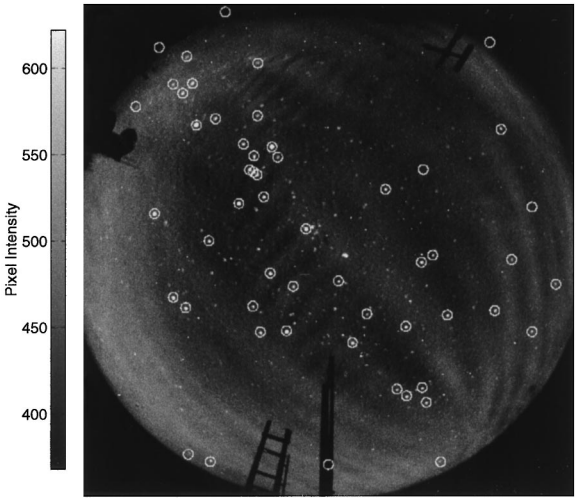

Fig. 7. Example of all-sky star calibration, using the image of Fig. 1; circles indicate the computed positions of all stars of magnitude greater than 1 within the field of view.

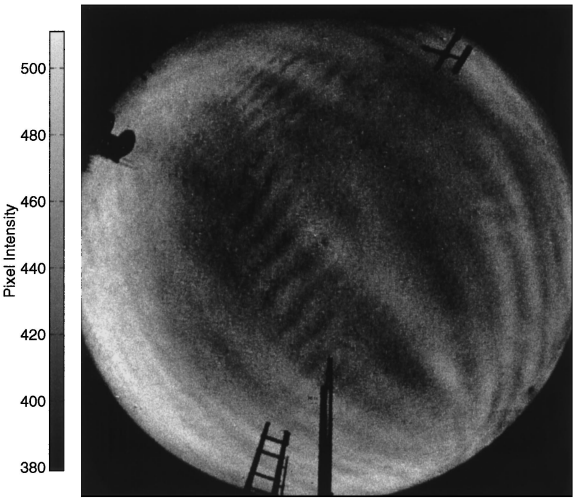

Fig. 8. Example illustrating star removal algorithm applied to Fig. 1. A threshold of 20 pixel counts and a maximum star size of 12 pixels were used.

coordinate system is then given by the angle it makes with the y axis, as shown in Fig. 4:

$$az = \tan^{-1}\left(\frac{x}{y}\right). \tag{5}$$

C. All-Sky Spatial Calibration

For the large-field information present in the all-sky data, accurate spatial calibration is essential. We can achieve this by using the stars in each image as known reference points in the sky.[28] Spatial calibration provides the necessary a and b coefficients in Eq. (2) for mapping the original image to standard coordinates. We determine the coefficients by performing a least-squares fit using the measured position of the stars in the original image and their positions in standard coordinates (derived from the right ascensions and declinations of the stars, the image time, and the site latitude and longitude).

Figure 7 illustrates the results of spatial calibration applied to the all-sky image of Fig. 1. Using Eq. (2), we calculated the image coordinates for all stars of magnitude 1 or brighter with positive elevation angles at the time the image was recorded. To demonstrate the accuracy of this calibration, we drew circles centered around the position calculated for these stars. Examination of the figure shows that all the bright stars within the image are encompassed by these circles. The mean distance of the calculated position of each star from its true location in the image was found to be less than 1 pixel. When the a and b coefficients are determined from any one image in a data set, they can be applied to all the images in the data set provided that the camera is not moved.

D. Star Removal

When an image has been calibrated, it is beneficial to remove the stars because they can cause streaking when an image is projected onto geographic coordinates and when images are averaged for flat fielding (see Section 2.F). We have developed a simple yet effective algorithm for removing stars while leaving the remainder of the image data essentially untouched. The basic premise behind the algorithm is that stars exhibit sharp, localized changes in intensity, the width of which are determined by the point-spread function of the system, while airglow features exhibit much more gradual changes. The key, however, is that the changes must occur in both the i and the j directions of the array. This algorithm seeks out such changes and replaces the stars with interpolated values from the surrounding pixels.

The algorithm scans an image line by line, looking for intensity changes of greater than a certain threshold. When such a change is detected, it continues to scan until the intensity value returns to within a threshold of the background. If, however, the intensity does not return to the background airglow level within a certain number of pixels (corresponding to the largest reasonable size of the stars in the image), the feature is considered too large to be a star and is disregarded. Because stars may not fall exactly on an integral number of pixels, there will be some leakage into the neighboring pixels. To account for this, the pixels immediately before and after a star is detected are also considered to be influenced by the star. When a star has been found, its corresponding intensity values are replaced by a linear fit of the surrounding pixels.

After the algorithm completes scanning the rows, it follows the same procedure with the columns. If a pixel's intensity is modified in both the row and the column scans, the final intensity is the average of the two values. If a pixel was not modified in both scans, it reverts back to its original value. Figure 8 shows the result of this processing as it is applied to the OI (557.7 nm) data in Fig. 1. In this example, the threshold pixel intensity value used to detect

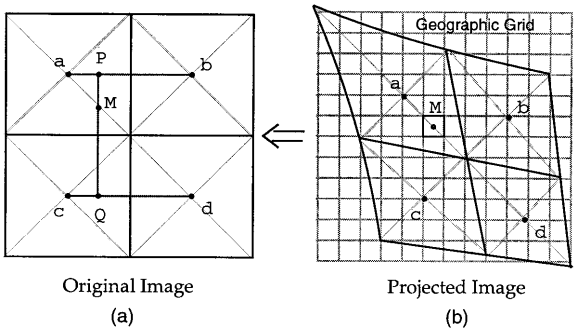

Fig. 9. Illustration showing method used to interpolate between the projected image on the geographic grid and the original image pixels; M denotes the grid element for which the intensity is to be estimated.

stars was 20 counts, and the maximum star width was assumed to be 12 pixels. The efficacy of this algorithm for removing stars without affecting the airglow data is readily apparent. The algorithm is equally effective in removing pointlike defects (hot pixels) in the CCD chip as well as bright pixels resulting from cosmic ray events. In principle, the removal of objects (such as the antennas and towers) in the low elevation field of view can be accomplished in a similar fashion, but the interpolation becomes much more involved and, as will be shown later, is not usually necessary.

E. All-Sky Projection onto a Uniformly Spaced Grid

In Section 2.B the transformation from the original image coordinates to the geographic coordinates was described. This transformation, often termed unwarping, is necessary for standard spectral analysis techniques that require uniform sampling of the data. Because the regularly sampled points in the geographic projection will not, in general, map exactly onto the center of the pixels in the image coordinates, some form of interpolation is necessary. This point is illustrated in Fig. 9, which shows the relationship between the original image pixels and their footprints projected onto a geographic grid.

We have experimented with several interpolation techniques, incorporating forward and backward mapping, and have determined that for our purposes a backward mapping followed by bilinear interpolation is most suitable. A short description of the method follows.

A point M (see Fig. 9) in the geographic map is converted to azimuth and elevation using Eqs. (4) and (5). The point is then transformed to standard coordinates with Eq. (3), and its corresponding position in the original image is determined with Eq. (2). Because this point does not lie exactly at the center of an image pixel, adjacent pixels need to be interrogated to estimate its value. A standard bilinear interpolation is performed by first linearly interpolating between points a and b to find the intensity value at P and linearly interpolating between points c and d to find the intensity value at Q. An estimate for the pixel value at M is then given by linearly interpolating between P and Q. This procedure is repeated for every point in the geographic grid [see Fig. 9(b)].

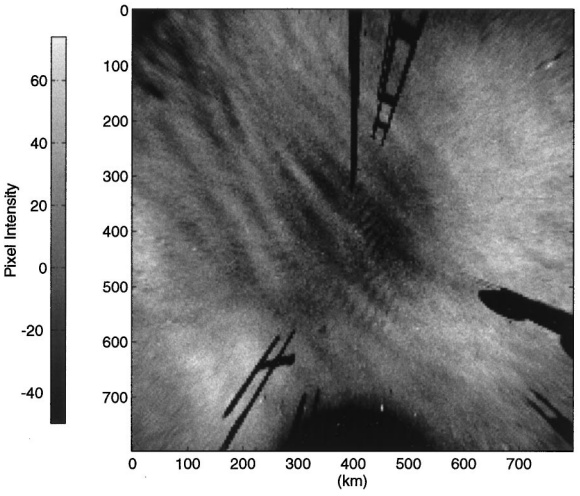

Fig. 10. Unwarped image showing results of projecting Fig. 8 onto a geographic grid; in this example, an area corresponding to 800 km × 800 km has been mapped with a pixel resolution of 2 km/pixel.

Figures 10 and 11 show two examples of unwarping all-sky images in this manner. In Fig. 10, a large area of the processed image (Fig. 8), corresponding to ~640,000 km^2 at the OI airglow layer, is mapped with an assumed emission altitude of 96 km. As expected, the small-scale waves are seen mainly over a limited geographic area within ~200 km radius of zenith. In comparison, the large-scale wave pattern is shown to be much more spatially extensive; however, even it does not appear to occupy the whole projection. This is due to the difference in the tangential and the radial resolution (see Fig. 3). The net effect in this case is that at low elevations the wave crests are visible in the northwest corner of the map (where they are oriented tangentially) but are more difficult to see in the southwest and northeast corners (where they are oriented radially). Never-

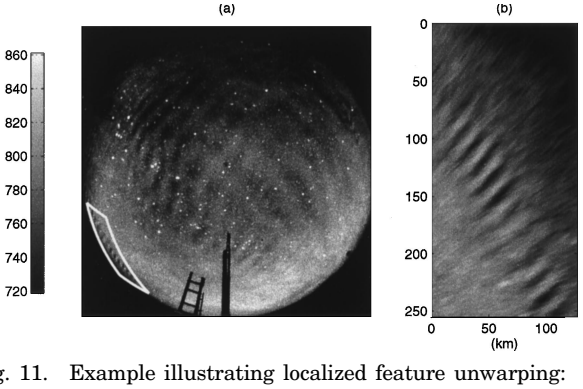

Fig. 11. Example illustrating localized feature unwarping: (a) image taken at 10:19 UT on the same night as Fig. 1, showing small-scale waves to the southeast at extremely low elevation; (b) unwarped image corresponding to the area indicated by the white border.

theless, the unwarping clearly shows the true quasilinear nature of the wave pattern.

Figure 10 also illustrates that the selection of the area to unwarp is dependent on what type of information is sought. For very short wavelength features (typically 5–15 km), it is better to concentrate the analysis over an area near the center of the image (thus allowing for a higher spatial resolution); longer wavelength features (a few tens of kilometers) can be analyzed with a lower spatial resolution and out to a much greater range from zenith. For significantly longer wavelength features (up to a few hundred kilometers), this method can be used to unwarp out to even larger ranges (approaching the horizon), but the presence in the near field of obstacles such as the antenna and the microwave tower in this example often limit the field.

Figure 11(a) shows a second example of airglow structure recorded on the same night as Fig. 1, when small-scale waves (~20-km horizontal wavelength) were observed close to the horizon. To further illustrate the power of the unwarping technique, we mapped the area that encompasses the structure (indicated by the white border). The resultant image [Fig. 11(b)] clearly shows at least 12 linear wave crests, enabling accurate measurements of their horizontal wavelength. With previous techniques to investigate such a wave pattern this measurement would have been extremely difficult.

F. Flat Fielding the All-Sky Image

Before we discuss the determination of gravity wave parameters, we consider a practical method for flat fielding the data to investigate relative intensity variations in the airglow (i.e., the ratio of the amplitude of the signal perturbation induced by the waves over the mean airglow signal, $\delta I/\bar{I}$). One common form of flat fielding is the use of a Lambertian-surface image of a white, uniformly illuminated dome for estimating the lens function. This method, however, fails to correct for the Van Rhijn effect (line-of-sight enhancement of the airglow signal resulting from an increase in the optical path length through the emission layer when viewed at low elevations) that is present in the image data. For this reason we describe an alternate method and, although it is not necessary for measurements of horizontal wavelength or phase speed, it is essential for estimating the power in the monochromatic wave components.

For meaningful determinations of $\delta I/\bar{I}$, it is important to make background image measurements alongside the airglow measurements to assess contamination of the data by sources other than the airglow. The OI (557.7 nm) and Na (589.2 nm) line emissions are ideally suited for these studies because the images are taken with an optical filter with a very narrow passband encompassing the emission line (see Table 1). A background image for these narrowband signals is achieved by the measurement of the sky emissions with a filter of approximately the same bandwidth but centered just off the emission line in a clean part of the sky spectrum. Background images usually have the same exposure time and are taken in close succession to the signal image. In comparison, accurate background corrections for the broadband near-infrared OH emission are significantly more difficult to achieve.

The sky signal S is assumed to be composed of a mean airglow signal $\bar{I}$ and the airglow signal perturbation δI. This signal is contaminated by noise from the stars, N_{stars}, and from other sky sources, N_{sky}, primarily resulting from continuum emission and aerosol scattering:

$$S = \bar{I} + \delta I + N_{\text{sky}} + N_{\text{stars}}. \tag{6}$$

To account for the competing effects of optical vignetting (which results in a significant reduction in the light throughput at the edge of the field of view) and Van Rhijn enhancement, we include the operator $H(i, j)$ that modifies the signal incident on the CCD. The effects of electronic noise in the CCD, including readout and thermal noise, are represented by N_{elec}. The resultant image A is then given by

$$A = H(i, j)(\bar{I} + \delta I + N_{\text{sky}} + \mathrm{N}_{\text{stars}}) + N_{\text{elec}}. \tag{7}$$

The background image can be modeled similarly as follows:

$$B = H(i, j)(N_{\text{sky}} + N_{\text{stars}}) + N_{\text{elec}}. \tag{8}$$

Examinations of dark images (i.e., exposures with the lens cap on) have revealed that most of the power in the readout and thermal noise is in dc, and therefore we make the approximation that N_{elec} is constant for fixed exposure times. Furthermore, we make the assumption that because the data image and its corresponding background image are taken within a short time of each other (usually within 1–2 min), they will effectively have the same sky noise contribution. Owing to the sequential nature of the measurements, however, there occurs a slight displacement in the star positions between the data image and its background; therefore we cannot assume that N_{stars} is the same in both images. To account for this, each data and background image is processed with the algorithm in Section 2.D for removing the stars, resulting in

$$A_{ns} = H(i, j)(\bar{I} + \delta I + N_{\text{sky}}) + N_{\text{elec}}, \tag{9}$$

$$B_{ns} = H(i, j)(N_{\text{sky}}) + n_{\text{elec}}, \tag{10}$$

where the subscript ns denotes images with the stars removed. Subtracting B_{ns} from A_{ns} and assuming that N_{elec} is constant and N_{sky} is the same in both images creates a background-corrected image BC:

$$BC = A_{ns} - B_{ns} = H(i, j)(\bar{I} + \delta I). \tag{11}$$

Because the airglow perturbation δI is not stationary, we may average out the effects of the waves by averaging together a series of background-corrected images, resulting in an average image AV:

$$AV = \overline{BC} = H(i, j)\bar{I}. \tag{12}$$

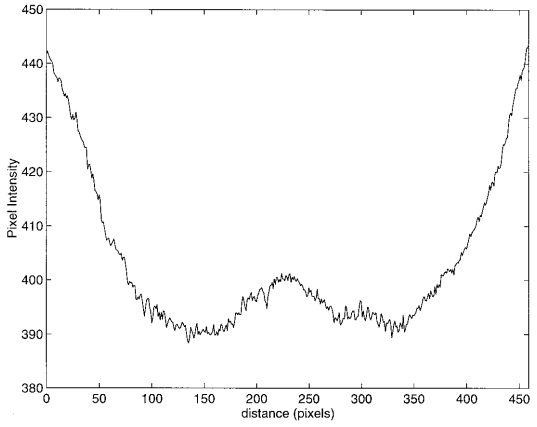

Fig. 12. Scan of averaged image (AV) showing the combined effects of lens vignetting and Van Rhijn enhancement on the all-sky image profile.

Figure 12 shows a scan across an example AV image we obtained by averaging 15 images spanning approximately 1 h. The contributions of lens vignetting and Van Rhijn are apparent and must be accounted for when the power in the various signal components are estimated. To account for gradual changes in the mean airglow signal $\bar{I}$ during a night's observations (due to tides and large-scale gravity waves), a set of AV images is usually created. Because $H(i, j)$ is unity at zenith, we can estimate the mean airglow signal $\bar{I}$ by measuring the zenith intensity of AV. The flat-fielded image FF is then given by

$$FF = \bar{I} + \delta I = \frac{BC}{AV}\bar{I}. \tag{13}$$

However, for estimating the fractional intensity change induced in the airglow emission by the gravity waves $\delta I/\bar{I}$, it is not necessary to determine completely the flat-fielded image because this can be found from the ratio of Eq. (11) and Eq. (12):

$$\frac{\delta I}{\bar{I}} = \frac{BC}{AV} - 1. \tag{14}$$

Figure 13 shows the results of this processing applied to the original image of Fig. 1. This $\delta I/\bar{I}$ image is ready for 2-D FFT. The two areas indicated by the black borders are the subjects of the analysis in Section 3.

3. Determination of Gravity Wave Parameters

Because we have processed the all-sky images, it is now possible to determine the horizontal wave parameters directly with standard 2-D FFT analysis. The advantage of this method is that measurements of all of the monochromatic features present in the data are now possible.

To create clean, well-defined peaks in the transform, we removed any linear trends associated with gradual variations in $\bar{I}$ across the field of view by fitting a plane to the $\delta I/\bar{I}$ image and then subtracting

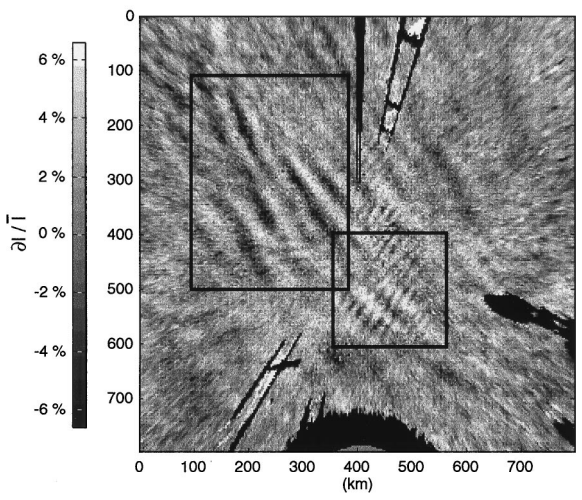

Fig. 13. Unwarped $\delta I/\bar{I}$ image corresponding to data from Fig. 1; black features are remnants of near-field antennas and other structures evident along the horizon in Fig. 1.

it. A 2-D Welch window is then applied to the data to minimize sidelobes in the frequency spectrum.[29]

We can investigate gravity wave content in any part of the image by isolating the region of interest, taking the 2-D FFT of the selected region, and investigating peaks in the squared magnitude of the frequency spectrum. Figure 14 shows two examples of this technique applied to the $\delta I/\bar{I}$ image of Fig. 13. Two regions were selected: one, indicated by the rectangle, contains the large-scale wave motion; and the second, indicated by the square, isolates most of the smaller-scale waves. Images (a) and (d) in Fig. 14 reproduce the regions of interest. The color plot (b) shows the computed squared magnitude of the 2-D FFT of (a). Owing to the symmetry of the FFT of real data, two mirror-image peaks in the power spectrum are evident at (± 0.021 km^{-1}, ∓ 0.012 km^{-1}), corresponding to the large-scale quasi-monochromatic wave structure present in (a). We can determine the horizontal wavelength of these waves by computing the inverse of the distance of the peak from the origin, and it was found to be 47 km ± 3 km. The direction of propagation of the wave is given (with a 180° ambiguity, again owing to the symmetry of the FFT) by the position of the peak in this k-space diagram (in this case the wave motion was progressing on a heading of either $-125°$ or 55°).

To further investigate the spatial frequencies present in this wave motion, we can isolate the peaks in the FFT to reconstruct the image with just those frequencies, corresponding to the quasi-monochromatic wave features. Figure 14(c) shows the reconstructed image of the large-scale waves shown in Fig. 14(a). The similarity between the prominent features in both images is clearly evident, indicating we have correctly identified the spatial frequencies associated with this wave. In comparison, the color plot [Fig. 14(e)] shows the spectral components associated with the waves present in image (d). Three distinct peaks are evident, one corre-

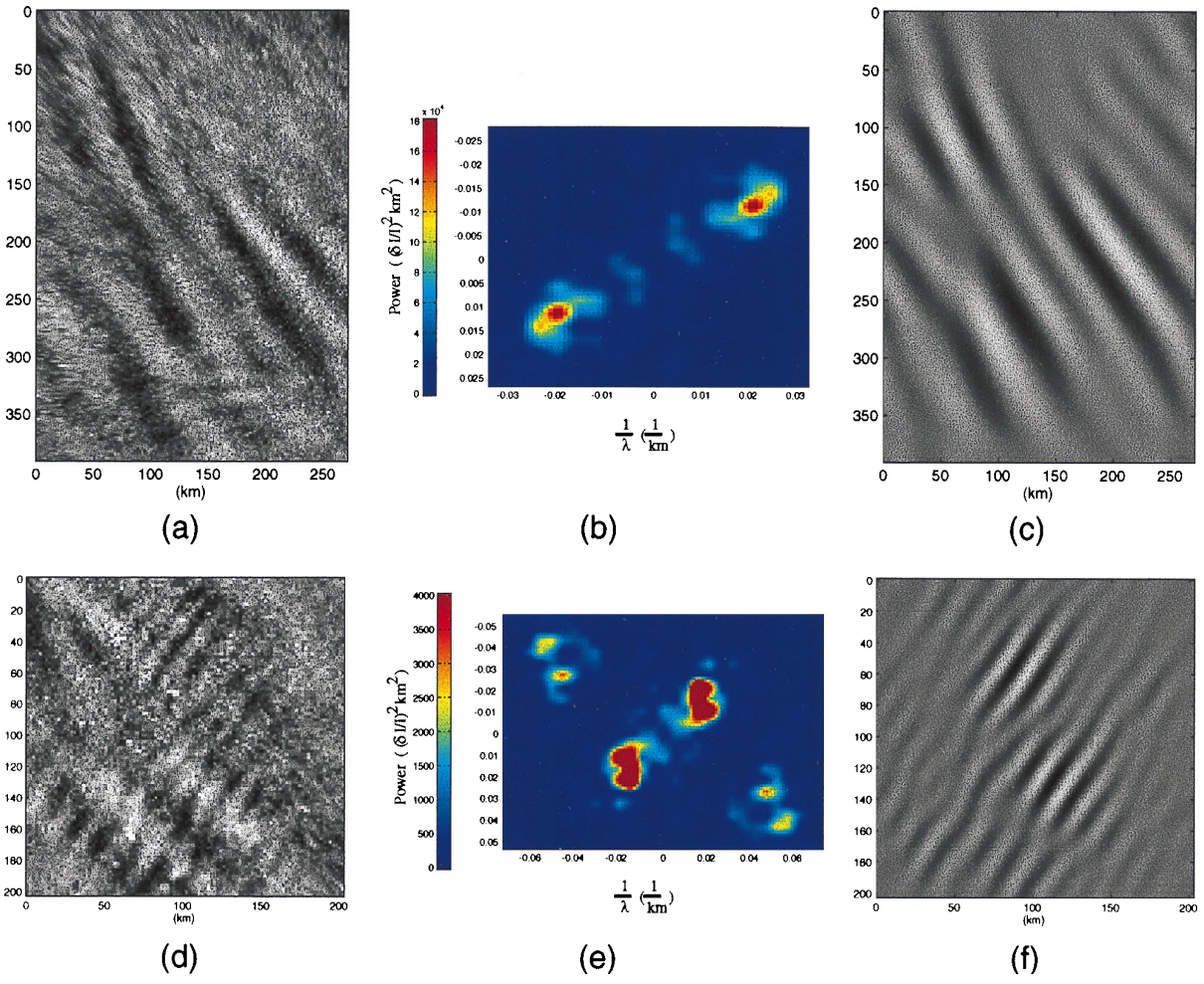

Fig. 14. Two examples illustrating 2-D FFT analysis of airglow data and image reconstruction: (a)–(c) a subsection of Fig. 13 (indicated by the rectangular border) that isolates the large-scale waves along with the 2-D FFT and a reconstruction of the wave pattern, corresponding to just those frequencies in the peak of the FFT; (d)–(f) a similar situation for the analysis of the small-scale waves (indicated by the square border in Fig. 13).

sponding to the larger-scale wave discussed above and two resulting from the smaller-scale waves, both of which are almost orthogonal to the larger-scale wave. Orthogonal wave motions of this type are of considerable interest because they are observed more frequently than would be expected by chance, suggesting a causal relationship.[30] In this case, the apparent splitting of the peaks for the small-scale waves is suggestive of a nonlinear wave interaction (this point is discussed in further detail in Section 4). The reconstruction of the small-scale waves is shown in Fig. 14(f) and was obtained by incorporating only the two small-scale peaks present in the FFT. The effect of this is to remove the large-scale wave from the reconstructed image, which enables clearer examination of the small-scale components.

Two methods are available to determine the periods (and hence phase speeds) of the waves present in these data. Using a sequence of images, we can plot the phase at each peak as a function of time. Figure 15(a) illustrates this method for the large-scale peak. The trend is very nearly linear, indicating uniform

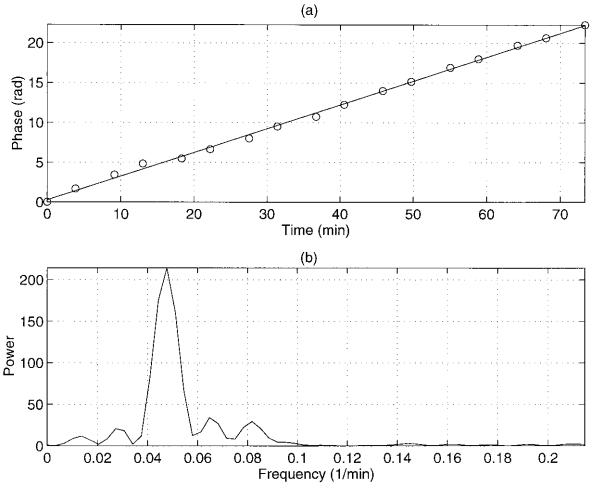

Fig. 15. Plots showing (a) the variation of phase of the spectral peak of the large-scale wave component with time; the slope of the linear least-squares fit to the data gives the period of 21.0 min, and (b) illustrates an alternative method for determining the period from the same data; a 1-D FFT is taken of the complex-valued data at the peak of the 2-D FFT. The peak indicates the wave frequency.

Table 2. Gravity Wave Parameters Derived from 2-D FFT Analysis

Wave Feature	λ_H (km)	az (deg)	τ (min)	$\lvert v_H \rvert$ (m/s)	$\delta I/\bar{I}$ (%)
Large-scale	47 ± 3	−125 ± 2	21.0 ± 0.2	37 ± 2	8.9
Small-scale$_a$	20 ± 1	124 ± 2	9.1 ± 0.2	37 ± 1	2.7
Small-scale$_b$	15.1 ± 0.5	130 ± 3	—[a]	—[a]	3.9

[a]Owing to the temporary nature of the small-scale$_b$ waves, there were insufficient data to determine their wave period and phase velocity.

phase motion of 37 ± 1 m/s. The slope of this line yields the wave period, which we have determined, using a linear least-squares fit to the data (solid line), to be 21.0 ± 0.2 min. The sign of the slope resolves the ambiguity in the direction of motion, indicating in this case wave progression toward the southwest (i.e., −125°).

The second method of estimating the wave period involves taking the one-dimensional (1-D) FFT in time of the complex 2-D FFT in space. The peaks in the squared magnitude of the 1-D FFT then correspond to the wave frequencies present in the data. Figure 15(b) shows the 1-D FFT for the large-scale wave. A single, well-defined peak is clearly evident at 0.048 min^{-1}, corresponding to a wave period of 20.9 min. Because this is a FFT of complex data, there is no symmetry between negative and positive frequencies, and the sign of the frequency of the peak (positive in this case) again resolves the ambiguity in the direction of motion. Table 2 lists the wave parameters we have computed for the waves present in this data set.

4. Discussion and Summary

To date, almost all of the short-period gravity wave measurements reported in the literature have been made by the measurement of the spatial separations and motion of the most prominent wave forms present in the original data sequence. This requires accurate visual identification of the wave motions by the operator and has consequently been applied only to high contrast, prominent wave forms.

The analysis techniques we have developed here have proved to be well suited to investigating the types of quasi-monochromatic wave events that are often recorded in airglow image data, including complex data containing more than one wave event. Our algorithms have been incorporated into a Matlab-based graphical user interface, providing a powerful interactive capability for investigating all-sky image data. By accurately unwarping the image, we have now made the analysis of very small scale waves (<20 km horizontal wavelength) practical over a significant portion of the sky (~480,000 km^2), and larger-scale waves can be analyzed out to much larger radii (limited by the presence of near-field objects in the image). By regridding the data, we are able to perform a 2-D FFT analysis on localized wave features that occur almost anywhere in the all-sky field of view. In contrast, previous Fourier investigations have focused on near-zenith measurements and have thus failed to take advantage of a large part of the airglow information.[11] The capability to navigate around the ground map in our analysis technique frees us from this constraint and permits maximum use of the all-sky information.

Comparison measurements with the classical spatial analysis technique outlined by Hapgood and Taylor[25] indicate that the errors in determination of the horizontal wavelength are comparable and are typically low (~1–2 km). Measurements of the apparent wave phase speed and direction of motion with the spectral analysis yield uncertainties somewhat lower than those typically achieved with spatial analysis methods (especially for less contrasted wave motions). The main reasons for this are probably the difficulties encountered by the operator in tracing accurately the motion of the wave pattern during analysis. The Fourier technique mitigates this problem through not requiring operator identification of specific wave features for the determination of wave period. This method provides for consistency and repeatability, which has not previously been available, in the wave parameter determination.

In a recent paper Taylor *et al*. suggested a mechanism whereby two large-scale waves that are progressing on similar azimuths may interfere and generate small-scale wave patterns that would appear almost orthogonal to the larger-scale waves.[30] If this were the case for the data presented here, we would expect to see two peaks in the power spectrum associated with the larger-scale waves and no smaller-scale components because they are simply the manifestation of the interference of the two larger waves. The occurrence of the smaller-scale peaks for this data set suggests that an alternative explanation is needed. The splitting of the peaks that correspond to the small-scale waves is suggestive of a nonlinear wave–wave interaction. If the airglow disturbance had been produced by the product of two waves (one low frequency and one high frequency, both propagating at similar azimuths), this is precisely the type of spectrum we would expect to see. Fritts *et al*. have investigated the properties of convective instabilities associated with the breakdown of large-scale waves.[31] Their model indicates that short-lived, small-scale waves oriented approximately orthogonal to the large-scale wave can be produced by gravity wave breakdown. This mechanism could possibly explain these data; however the model predicts scale sizes that are significantly smaller (~5 km) than those observed on this night (see Table 2).

A natural extension of the all-sky analysis capability discussed here is the investigation of power law trends in the horizontal spectra of the image data. Several theories have been proposed to account for wave saturation and dissipation in the upper mesospheric and the lower thermospheric regions, which predict the form of the power law trends.[32–34] Quasi-monochromatic waves evident in the airglow emissions may simply be superposed on this turbulent background or may form part of the nonlinear actions that create the power law dependence of wave properties on the horizontal wave number k. Using a narrow-field airglow imager (60° field of view) centered on the zenith, Hecht *et al*. have estimated the spectral slope and found it to be between -2.5 and -3 (Ref. 8). However, the limited field of view restricted the spectral range of these measurements to wavelengths less than 110 km. For all-sky image data, the available spectral range is significantly larger, and we are currently investigating methods to use these large-field data for accurate spectral slope estimates.

In summary, this paper describes how to use the full potential of digital all-sky airglow data for quantitative spectral investigations of quasi-monochromatic gravity waves (periods $\leq$1 h). By automating most of the processing associated with the wave parameter determination (wavelength, velocity, period, $\delta I/\bar{I}$), we have developed an efficient analysis technique that can now be used for in-depth studies of complex image data. Furthermore, this analysis facilitates long-term studies that promise to provide a wealth of information on seasonal and geographic variability important for improving current atmospheric models.

We are grateful to ThermoTrex Corporation for arranging our use of the U.S. Department of Energy facilities, Haleakala, Maui, Hawaii, for the airglow measurements. The Utah State University image measurements and analysis were supported by National Science Foundation grants ATM-9302844 and ATM-9525815 and by the U.S. Air Force, Phillips Laboratory, contract F19628-93-C-0165, as part of the Structured Optical Atmospheric Radiance (SOAR) program. F. J. Garcia was supported under a National Science Foundation Graduate Fellowship for much of this study; he also acknowledges H. C. Torng, Cornell University, for his support.

References

1. V. I. Krassovsky and M. V. Shagayev, "On the nature of internal gravity waves observed from hydroxyl emission," Planet. Space Sci. **25,** 200–201 (1977).
2. N. M. Gavrilov and G. M. Shved, "Study of internal gravity waves in the lower thermosphere from observations of the nocturnal sky airglow [OI] 5577 Å in Ashkhabad," Ann. Geophys. **38,** 789–803 (1982).
3. H. Takahashi, P. P. Batista, Y. Sahai, and B. R. Clemesha, "Atmospheric wave propagations in the mesopause region observed by the OH (8,3) band, NaD, O_2 (8645 Å) band and OI 5577 Å nightglow emissions," Planet. Space Sci. **43,** 381–384 (1985).
4. H. K. Myrabø, C. S. Deehr, R. A. Viereck, and K. Henriksen, "Polar mesopause gravity waves in the sodium and hydroxyl night airglow," J. Geophys. Res. **92,** 2527–2534 (1987).
5. M. J. Taylor, M. A. Hapgood, and P. Rothwell, "Observations of gravity wave propagation in the OI (557.7 nm), Na (589.2 nm) and the near-infrared OH nightglow emissions," Planet. Space Sci. **35,** 413–427 (1987).
6. R. P. Lowe, K. L. Gilbert, and D. N. Turnbull, "High latitude summer observations of the hydroxyl airglow," Planet. Space Sci. **39,** 1263–1270 (1991).
7. S. P. Zhang, R. H. Wiens, and G. G. Shepard, "Gravity waves from O_2 nightglow during the AIDA'89 campaign, II, Numerical modeling of the emission rate/temperature ratio, η," J. Atmos. Terr. Phys. **54,** 377–395 (1992).
8. J. H. Hecht, R. L. Walterscheid, and M. N. Ross, "First measurements of the two-dimensional horizontal wave number spectrum from CCD images of the nightglow," J. Geophys. Res. **99,** 11,449–11,460 (1984).
9. G. R. Swenson and S. B. Mende, "OH emissions and gravity waves (including a breaking wave) in all-sky imagery from Bear Lake, Utah," Geophys. Res. Lett. **21,** 2239–2242 (1994).
10. P. R. Fagundes, H. Takahashi, Y. Sahai, and D. Gobbi, "Observations of gravity waves from multispectral mesospheric nightglow emissions observed at 23 °S," J. Atmos. Terr. Phys. **57,** 359–405 (1995).
11. M. J. Taylor and F. J. Garcia, "A two-dimensional spectral analysis of short period gravity waves imaged in the OI (557.7 nm) and near-infrared OH nightglow emissions over Arecibo, Puerto Rico," Geophys. Res. Lett. **22,** 2473–2476 (1995).
12. J. R. Holton, *An Introduction to Dynamic Meteorology*, Vol. 23 of International Geophysical Series (Academic, San Diego, Calif., 1979).
13. R. R. Garcia and S. Solomon, "The effects of breaking gravity waves on the dynamics and chemical composition of the mesosphere and lower thermosphere," J. Geophys. Res. **90,** 3850–3868 (1985).
14. I. M. Reid and R. A. Vincent, "Measurements of the horizontal scales and phase velocities of short period mesospheric gravity waves at Adelaide, Australia," J. Atmos. Terr. Phys. **49,** 1033–1048 (1987).
15. D. C. Fritts and T. E. VanZandt, "Spectral estimates of gravity wave energy and momentum fluxes, I: Energy dissipation, acceleration, and constraints," J. Atmos. Sci. **50,** 3685–3694 (1993).
16. M. J. Taylor and M. J. Hill, "Near-infrared imaging of hydroxyl wave structure over an ocean site at low latitudes," Geophys. Res. Lett. **18,** 1333–1336 (1991).
17. G. R. Swenson, M. J. Taylor, P. J. Espy, C. Gardner, and X. Tao, "ALOHA-93 measurements of intrinsic AGW characteristics using airborne airglow imager and groundbased Na Wind/Temperature lidar," Geophys. Res. Lett. **22,** 2841–2844 (1995).
18. M. J. Taylor, M. B. Bishop, and V. Taylor, "All-sky measurements of short period waves imaged in the OI (557.7 nm), Na (589.2 nm), and near infrared OH and O_2 (0,1) nightglow emissions during the ALOHA-93 campaign," Geophys. Res. Lett. **22,** 2833–2836 (1995).
19. Q. Wu and T. L. Killeen, "Seasonal dependence of mesospheric gravity waves (<100 km) at Peach Mountain Observatory, Michigan," Geophys. Res. Lett. **23,** 2211–2214 (1996).
20. A. W. Peterson and L. M. Kieffaber, "Infrared photography of OH airglow structures," Nature **242,** 321–322 (1973).
21. G. Moreels and M. Herse, "Photographic evidence of waves around the 85-km level," Planet. Space Sci. **25,** 265–273 (1977).
22. J. Crawford, P. Rothwell and M. J. Taylor, "Airglow TV" sidebar in "ASSESS 2: a simulated mission of *Spacelab* (Review Article)," Nature **275,** 17 (1978).

23. E. B. Armstrong, "The association of visible airglow features with a gravity wave," J. Atmos. Terr. Phys. **44,** 325–336 (1982).
24. M. J. Taylor, P. J. Espy, D. J. Baker, R. J. Sica, P. C. Neal, and W. R. Pendleton Jr., "Simultaneous intensity, temperature, and imaging measurements of short period structure in the OH nightglow emission," Planet. Space Sci. **39,** 1171–1188 (1991).
25. M. A. Hapgood and M. J. Taylor, "Analysis of airglow image data," Ann. Geophys. **38,** 805–813 (1982).
26. B. S. Lanchester, "Relation between discrete auroral forms and magnetic field disturbances," Ph.D. dissertation (Department of Physics, University of Southampton, Southampton, UK, 1985).
27. K. H. Lloyd, "Concise method for photogrammetry of objects in the sky," Weapons Research Establishment Technical Note 72, 1971 (Australian Defence Scientific Service, Canberra, Australia).
28. W. Smart, *Spherical Astronomy*, 5th ed. (Cambridge U. Press, Cambridge, UK, 1965).
29. W. H. Press, S. A. Teukolsy, W. T. Vetterling, and B. P. Flannery, *Numerical Recipes in C* (Cambridge U. Press, Cambridge, UK, 1992).
30. M. J. Taylor, D. C. Fritts, and J. R. Isler, "Determination of horizontal and vertical structure of an unusual pattern of short period gravity waves imaged during ALOHA-93," Geophys. Res. Lett. **22,** 2837–2840 (1995).
31. D. C. Fritts, J. R. Isler, G. Thomas, and O. Andreassen, "Wave breaking signatures in noctilucent clouds," Geophys. Res. Lett. **20,** 2039–2042 (1993).
32. E. M. Dewan and R. E. Good, "Saturation and the 'universal' spectrum for vertical profiles of horizontal scalar winds in the atmosphere," J. Geophys. Res. **91,** 2742–2748 (1986).
33. C. O. Hines, "The saturation of gravity waves in the middle atmosphere, II, Development of Doppler-spread theory," J. Atmos. Sci. **48,** 1360–1379 (1991).
34. C. S. Gardner, "Diffusive filtering theory of gravity wave spectra in the atmosphere," J. Geophys. Res. **99,** 20,601–20,622 (1994).